The Role of Horizontal Boundaries in Parameter Sensitivity and Decadal-Scale Variability of Coarse-Resolution Ocean General Circulation Models*

MICHAEL WINTON†

Joint Institute for the Study of the Atmosphere and Ocean, University of Washington, Seattle, Washington

(Manuscript received 28 November 1994, in final form 4 May 1995)

ABSTRACT

Coarse-resolution f-plane and β-plane frictional geostrophic models are used to study the response to restored surface buoyancies and fixed surface buoyancy fluxes. With restored surface buoyancies it is found that the overturning and meridional buoyancy transport generally follow the scaling from thermal wind and vertical advective–diffusive balance. When maximum midbasin rather than maximum overall streamfunction is used as the metric, the sensitivity of overturning magnitude to vertical diffusivity agrees quite closely with that of a two-dimensional Rayleigh frictional model that follows an analogous scaling. This measure of meridional overturning, as well as the meridional buoyancy transport, also roughly follow the predicted $f^{-1/3}$ scaling and are relatively insensitive to variations in β and horizontal viscosity.

The sensitivity experiments indicate that the coarse-resolution model overturning and thermodynamic structure are well characterized by the adjustment of a uniformly rotating viscous fluid to boundaries parallel to the surface forcing gradient. This adjustment is examined in more detail with linear and nonlinear models. In stratified regions, thermal wind currents normal to the coast initiate the adjustment by forcing pycnocline depth anomalies in the coastal (horizontal) Ekman layer. These anomalies propagate around the coast in the Kelvin wave direction, setting up geostrophic currents parallel to the coast. In a model initialized with a high-latitude baroclinic jet, a warm (cold) boundary signal spreads around the poleward (equatorward) part of the basin, initiating geostrophic currents connecting the flow onto the coast in the east with that away from the coast in the west to form two gyres. The warm coastal signal propagates slowly along the weakly stratified polar wall. In steady circulations, strong damping inhibits warm signal propagation, and the warm water on the poleward part of the eastern coast is forced to downwell.

Self-sustaining decadal-scale oscillation is a robust feature of the models when forced with fixed buoyancy fluxes. This variability is inherently three-dimensional (it does not occur in a two-dimensional frictional model) and involves the periodic growth and decay of a baroclinic jet in the poleward eastern corner. Decay occurs when a jetlike disturbance, normal to the coast, propagates cyclonically around the basin replacing the cold water along the boundary with warm. Forcing of thermal wind currents normal to weakly stratified coasts and weak damping of the resulting propagating boundary disturbances are found to be conducive to oscillations.

1. Introduction

One of the primary physical elements that distinguishes the ocean's circulation from that of the atmosphere is the presence of horizontal boundaries. The purpose of this paper is to investigate 1) the role of these boundaries in producing the sensitivities and circulations of steady coarse-resolution ocean general circulation model (OGCM) solutions and 2) their potential role in decadal-scale internal variability. This is an effort to understand why the OGCMs exhibit the behaviors they do. A thorough understanding of the workings of the OGCMs is especially important because the long timescales of oceanic processes and the difficulty of collecting observations limit our ability to validate these models by comparison with natural experiments.

In this pursuit, it is useful to employ a range of models to isolate the behaviors in their simplest context. Our basic tool is a model that retains the full thermodynamics of the primitive equation models but simplifies the dynamics by eliminating vertical momentum diffusion and inertial terms (both time dependence and momentum advection). The formulation of this frictional geostrophic model is given in section 2. Winton (1994) investigated the sensitivity of a two-dimensional frictional model (a frictional geostrophic model without rotation) to variations in the vertical diffusivity. In section three, we build upon that study by comparing this sensitivity with that of the three-dimensional frictional geostrophic model. In particular, we are interested in whether the less than scale sensitivity found by Bryan (1987) is due to rotation or to ther-

* JISAO Contribution Number 302.

† UCAR Visiting Scientist.

Corresponding author address: Dr. Michael Winton, GFDL/NOAA, Princeton University, P.O. Box 308, Princeton, NJ 08542.
E-mail: mw@gfdl.gov

modynamics, and so characterized by the two-dimensional model. Additionally, we would like to address an apparent discrepancy between the $K_v^{1/3}$ sensitivity of meridional overturning and the $K_v^{2/3}$ sensitivity of poleward heat transport (see Bryan 1991). The standard scaling argument predicts a $K_v^{2/3}$ sensitivity for both of these quantities. It will be shown that high-latitude boundary processes contaminate the measure of overturning magnitude used by F. Bryan.

The sensitivities to variations in f, β, and horizontal viscosity A, and the buoyancy structure of experiments with various f-plane configurations in section 3 indicate that the adjustment of uniformly rotating viscous fluid to horizontal boundaries parallel to the forcing gradient is central to the behavior of the coarse-resolution OGCMs. This adjustment is explored in section 4 with the full nonlinear f-plane model and a linear shallow water counterpart. We focus upon the role of propagating boundary disturbances in the development of gyre circulations and the effect that damping of these disturbances has upon the steady solution.

Using a fixed flux boundary condition rather than the conventional surface restoring boundary condition, several researchers (Huang and Chou 1994; Chen and Ghil 1995; Greatbatch and Zhang 1995) have found internal decadal-scale variability similar to that found previously with mixed boundary conditions (Weaver and Sarachik 1991; Yin and Sarachik 1994). Greatbatch and Zhang (1994) argue that this kind of variability is the source of the decadal-scale variability in global coupled ocean–atmosphere climate simulations (Dellworth et al. 1993). The isolation of the variability in models with a single density component greatly simplifies its study. In section 5, the response to fixed buoyancy flux boundary conditions is studied with two- and three-dimensional models. The fact that the variability is well reproduced by an f-plane model allows us to explore it in a number of forcing and basin configurations in an attempt to find its root cause. A discussion of the results is presented in section 6.

2. The model

Our intent is to capture the essential behavior of the coarse-resolution primitive equation models in the simplest possible set of equations. Because coarse-resolution grids are many Rossby radii wide, we may neglect the momentum advection terms. The processes involved in the setup and variability of coarse-resolution model circulations have timescales long compared to a rotational period, and so the time-dependent terms may similarly be neglected. In coarse-resolution model runs, a large horizontal momentum diffusivity is used so that the grid will resolve the Munk western boundary layer of width $(A_h/\beta)^{1/3}$. A vertical momentum diffusivity on the same order as the tracer diffusivity is usually employed. Thus, for typical choices of these quantities, the vertical momentum diffusion term is also negligible since

$$A_v \approx 10^{-4}\ \mathrm{m^2\ s^{-1}} \ll \frac{H^2}{L^2} A_h$$

$$\approx 10^{-6} \times 10^{5}\ \mathrm{m^2\ s^{-1}} = 10^{-1}\ \mathrm{m^2\ s^{-1}}.$$

The model equations are then the frictional geostrophic set used by Colin de Verdiere (1988, 1989) and Winton (1993a,b):

$$f\mathbf{k} \times \mathbf{v} = -\nabla p + A\nabla^2\mathbf{v} \tag{2.1a}$$

$$\frac{\partial p}{\partial z} = b \tag{2.1b}$$

$$\nabla\cdot\mathbf{v} + \frac{\partial w}{\partial z} = 0 \tag{2.1c}$$

$$\frac{\partial b}{\partial t} + \mathbf{v}\cdot\nabla b + w\frac{\partial b}{\partial z} = K_h\nabla^2 b + K_v\frac{\partial^2 b}{\partial z^2} + Q_b\frac{H(z + 50\ \mathrm{m})}{50\ \mathrm{m}}, \tag{2.1d}$$

where f is the Coriolis parameter, $\mathbf{v}$ is the horizontal velocity vector ($u\mathbf{i} + v\mathbf{j}$), w is vertical velocity, b is buoyancy, p is pressure (normalized with a reference density), A is the horizontal viscosity coefficient, K_v and K_h are the vertical and horizontal tracer diffusivities, H is the Heaviside step function, and Q_b is the surface buoyancy flux; $\mathbf{i}$, $\mathbf{j}$, and $\mathbf{k}$ are the unit vectors in the zonal, meridional, and vertical directions, respectively. A convective adjustment is incorporated in K_v as an infinite vertical mixing in statically unstable columns. This mixing is implemented by the following procedure, performed every timestep after the buoyancy flux has been applied to the top 50-m grid layer: set a mixed layer buoyancy to the buoyancy of the top grid box then proceed downward mixing additional grid boxes into the mixed layer until the mixed layer buoyancy is greater than the grid box below or the bottom is reached. This one-pass procedure works because all static instability is forced from the surface and, without inertia, fluid parcels do not flow beneath less buoyant parcels.

The equations are solved in Cartesian coordinates on a β plane; that is, $f = f_0 + \beta(y - y_{\mathrm{mid}})$, where y_{mid} is the y coordinate of the basin middle. The standard geometry is a 5000-km square box, 4 km deep. There are 16 vertical grid levels. With the f plane ($\beta = 0$), channel configurations are also used. In channel f-plane configurations, only cross-channel viscosity is retained and (2.1a) is replaced by

$$f\mathbf{k} \times \mathbf{v} = -\nabla p + A\frac{\partial^2\mathbf{v}}{\partial y^2}$$

$$\text{or} \quad f\mathbf{k} \times \mathbf{v} = -\nabla p + A\frac{\partial^2\mathbf{v}}{\partial x^2}. \tag{2.1a′}$$

The former is used in channels that are reentrant in the x direction and the latter in channels reentrant in the y

direction. Writing the horizontal velocity as a complex number $u + iv$, (2.1a) and (2.1a′) become elliptic equations in a complex variable. Here (2.1a) is solved by successive over relaxation, and (2.1a′) by a simple tridiagonal matrix inversion.

We will investigate two kinds of surface buoyancy forcings. The first (used in sections 3 and 4) restores the buoyancy of the top grid layer to a reference profile:

$$Q_b = P\{2 \times 10^{-2}\ \mathrm{m\ s^{-2}}[1 + \cos(y\pi/L_y)] - b[z = -25\ \mathrm{m}]\}, \quad (2.2)$$

where P, the boundary condition piston velocity, is set to 1 m day^{-1}. This corresponds to the usual procedure used for thermal forcing in ocean-only simulations and is based upon a linearization of the surface fluxes expanded in air–sea temperature difference (Haney 1971). The second boundary condition (used in section 5) applies fixed surface buoyancy fluxes. It might correspond to a first approximation of the haline forcing of the ocean, but we will be using it here in simplified fluid dynamical experiments to determine natural modes of internal variability.

Even though the model is cast in terms of buoyancy, for ease of expression, thermal language shall be used in this paper—warm meaning buoyant, cold, less buoyant, and so on.

3. Adherence to scaling

Assuming scales from thermal wind balance, continuity, vertical advective–diffusive buoyancy balance, and a surface buoyancy range, Δb, from the restoring boundary condition

$$f\frac{\partial \mathbf{v}}{\partial z} = -\mathbf{k} \times \nabla b \Rightarrow \frac{U}{d} \approx \frac{\Delta b}{fL},$$

$$\nabla \cdot \mathbf{v} + \frac{\partial w}{\partial z} = 0 \Rightarrow \frac{U}{L} \approx \frac{W}{d},$$

and

$$w\frac{\partial b}{\partial z} = K_v\frac{\partial^2 b}{\partial z^2} \Rightarrow W \approx \frac{K_v}{d},$$

we can obtain scales for the pycnocline depth d, the horizontal velocity U, and the overturning streamfunction Ψ in the usual manner (Welander 1971; Bryan 1987):

$$d \approx \left[\frac{K_v L^2 f}{\Delta b}\right]^{1/3}, \quad U \approx \left[\frac{K_v}{L}\left(\frac{\Delta b}{f}\right)^2\right]^{1/3},$$

$$\Psi \approx UdL \approx \left[\frac{K_v^2 L^4 \Delta b}{f}\right]^{1/3}. \quad (3.1a,b,c)$$

The overturning streamfunction ψ is defined in terms of the (nondivergent) zonally integrated flow so that

$$\frac{\partial \psi}{\partial y} = \int_0^L w dx \quad \text{and} \quad \frac{\partial \psi}{\partial z} = -\int_0^L v dx.$$

The poleward buoyancy transport F_b scales as

$$F_b \approx \Psi \Delta b \approx \left[\frac{K_v^2 L^4 \Delta b^4}{f}\right]^{1/3}. \quad (3.2)$$

If the surface buoyancy flux is fixed rather than the buoyancy gradient, it must be equal, in steady state, to the interior buoyancy transport, and we can multiply (3.1c) by $\Psi^{1/3}$, substitute F_b for $\Psi\Delta b$, and take the result to the 3/4 power to obtain a scale for the overturning in terms of a fixed buoyancy flux (Huang and Chou 1994):

$$\Psi \approx \left[\frac{K_v^2 F_b L^4}{f}\right]^{1/4}. \quad (3.3a)$$

The scale for Δb follows from (3.2):

$$\Delta b \approx \left[\frac{F_b^3 f}{K_v^2 L}\right]^{1/4}. \quad (3.3b)$$

The frictional geostrophic model is now configured with $A = 2.5 \times 10^5\ \mathrm{m^2\ s^{-1}}$, $K_h = 5 \times 10^2\ \mathrm{m^2\ s^{-1}}$, $K_v = 5 \times 10^{-5}\ \mathrm{m^2\ s^{-1}}$, $f_0 = 10^{-4}\ \mathrm{s^{-1}}$, and $\beta = 2 \times 10^{-11}\ \mathrm{m^{-1}\ s^{-1}}$ for the sensitivity studies of the remainder of this section. A 20 by 20 horizontal grid is used giving a resolution of 250 km, which only marginally resolves the Munk western boundary layer [$(A/\beta)^{1/3} = 232$ km] and is far from resolving the horizontal Ekman layer [$(2A/f)^{1/2} = 71$ km]. This is in accordance with the usual parameter and grid resolution values used in coarse-resolution models (e.g., Bryan 1987).

Table 1 shows the sensitivity of meridional overturning and buoyancy transport to variations in K_v in the range of values suggested by tracer studies. The unparenthesized numbers are maximum streamfunction and buoyancy transport at $y = 2.5 \times 10^6$ m (midbasin). The streamfunction numbers in paretheses are the *basin* maximum streamfunction values, typically found at middepth near the polar wall. This measure shows considerably less K_v sensitivity than the midbasin measure.

TABLE 1. Maximum overturning and buoyancy transport sensitivity to K_v. Numbers are for midbasin except overturning in parentheses is *basin* maximum overturning.

K_v ($\mathrm{m^2\ s^{-1}}$)	Ψ ($10^6\ \mathrm{m^3\ s^{-1}}$)	$\Delta \ln\Psi/\Delta \ln K_v$	F_b ($10^4\ \mathrm{m^4\ s^{-3}}$)	$\Delta \ln F_b/\Delta \ln K_v$
10^{-5}	2.31 (6.58)		3.64	
		0.54 (0.35)		0.54
$5 \cdot 10^{-5}$	5.55 (11.5)		8.67	
		0.56 (0.39)		0.56
10^{-4}	8.19 (15.1)		12.8	

The reason for this is that it contains a large contribution from the boundary upwelling and downwelling, which dominate the vertical motion in the high-latitude part of the basin. These vertical motions are forced by a strong baroclinic zonal jet associated with convective layers, which deepen and cool going poleward. Figure 1 shows that the orientation of this jet becomes more zonal as K_v is increased. Thus, the western boundary upwelling and the eastern and polar boundary downwelling increasingly cancel each other in the zonally averaged meridional streamfunction, resulting in a reduced sensitivity to K_v. This alignment effect accounts for the result of F. Bryan, who found that the zonal overturning was proportional to $K_v^{2/3}$ while the meridional overturning was proportional to $K_v^{1/3}$. Bryan (1991) later showed that the heat transports at 25°N for these experiments were reasonably close to a $K_v^{2/3}$ scaling. This would seem to contradict the scaling (3.2) above since the density gradients are relatively fixed by the restoring boundary condition used in the experiments.

In fact, the basin maximum streamfunction is a poor measure of the thermodynamically important vertical motion because the large high-latitude upwelling occurs in regions with little or no vertical stratification (see Fig. 7a). It is noteworthy in this regard that the basin maximum streamfunction stays fixed at 1650-m depth rather than shallowing with the thermocline as it does in two-dimensional model experiments (Winton 1995). For these reasons the midbasin maximum is a better metric. In Table 1 it is shown to have a sensitivity in close agreement with that of the meridional buoyancy transport as expected from the scaling. Furthermore, a roughly $K_v^{0.55}$ scaling was also found in a two-dimensional Rayleigh friction model by Winton (1995). This model follows the same scaling argument with the Rayleigh friction parameter r playing the role of the Coriolis parameter f. This agreement indicates that the somewhat less than scale sensitivities are the result of thermodynamics rather than rotation or other dynamical effects. In any case, the adherence to scaling is quite good considering that the scaling argument does not consider the necessity of the vertical velocity approaching zero near the upper and lower boundaries.

What causes the shift in orientation of the high-latitude jet seen in Fig. 1? The jet's path is influenced by the placement of warm and cold features that extend through the entire water column. These features can be seen most clearly in plots of buoyancy at the bottom (Figs. 1b and 1d). In the low diffusivity case, the coldest water in the basin occurs in an unstratified column in the poleward western corner. The warmest deep water (formed by downwelling through weak stratification) is located in the poleward eastern corner. Thermocline water flows cyclonically around the cold feature onto the polar boundary and sinks west of the warm feature. In the high diffusivity case, the cold column is shifted eastward 2000 km along the polar boundary while the warm column is shifted just south of the poleward eastern corner. Now the cyclonic flow around the cold feature is more zonal and sinks upon reaching the eastern wall just poleward of the warm feature.

Now we turn our attention from the role of vertical diffusivity to the role of rotation in the scaling for the overturning. In the two-dimensional model of Winton (1995), the Rayleigh friction parameter r scales out of the equations and a scaling argument analogous to the one leading to (3.1c) gives $\Psi^* \sim k^{*2/3}$, where $k^* = K_v r L^2 (\Delta b H^3)^{-1}$ and H is the basin depth. The dimensional meridional overturning scale is then recovered from k^* and the timescale $t^* = rL^2(\Delta bH)^{-1}$,

$$\Psi = \frac{HL}{t^*}\Psi^* \approx \frac{HL}{t^*}k^{*2/3} = \left[\frac{K_v^2 L \Delta b}{r}\right]^{1/3}. \quad (3.4)$$

In the rotating case, the role of f is less straightforward as there are two other parameters which might plausibly provide resistance to meridional overturning, A and β. Furthermore, the velocity scale that is obtained from thermal wind relation is for the zonal velocity not the meridional velocity.

First, we examine the possibility that A or β might play a significant role in controlling the meridional overturning. A steady state without rotation ($f = \beta = 0$) has a maximum midbasin streamfunction of 104×10^6 m^3 s^{-1}. This large value is expected from the long timescale associated with horizontal friction; if we replace f^{-1} with the viscous timescale L^2/A in the scaling, the overturning scale increases by a factor of $(fL^2/A)^{1/3}$, about 22, roughly as observed. In conjunction with the standard f_0 and β, horizontal viscosity *increases* meridional overturning and buoyancy transport slightly. In experiments with doubled horizontal resolution (40×40), increasing A from 5×10^4 to 2.5×10^6 m^2 s^{-1} increased the midbasin maximum streamfunction and buoyancy transport by 4%. The pycnocline was slightly shallower and deep water slightly denser in the high viscosity case. These results are counter to the idea that an overly deep thermocline in coarse-resolution models is caused by large viscosity (Bryan 1987), although the presence of narrow straits might alter this result.

Next we turn to the role of β. Table 2 shows meridional overturning and buoyancy transports for experiments with β half of the standard value and set to zero. There is a 14% reduction in overturning and a 20% reduction in buoyancy transport when β is increased from zero to the standard value of 2×10^{-11} m^{-1} s^{-1}. The β effect, while important, is clearly not the main reason for the dramatic reduction in these quantities over their frictionally determined values. Table 3 shows the result of f-plane experiments with f increased and decreased from the standard value by factors of 10. The sensitivities are somewhat larger than the predicted $f^{-1/3}$ scaling. Thus, it appears that it is f

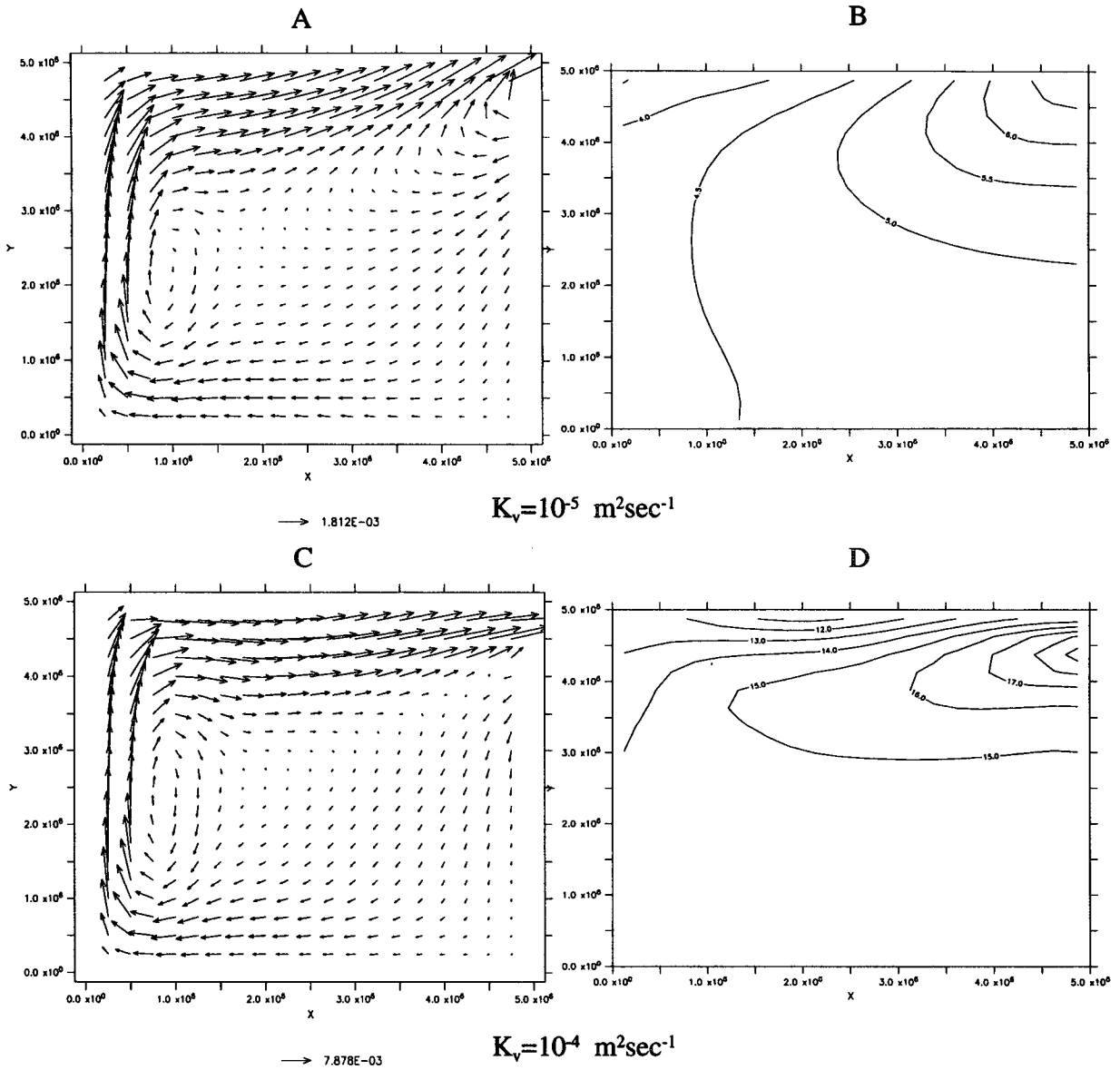

FIG. 1. Steady states with $K_v = 10^{-5}$ m^2 s^{-1} (a) and (b) and $K_v = 10^{-4}$ m^2 s^{-1} (c) and (d). Left panels are horizontal velocities (m s^{-1}) averaged from the surface to 1650-m depth (the depth of the maximum overturning streamfunction in both cases). Right panels are buoyancy at the bottom (10^{-4} m s^{-2}). The high-latitude jet becomes more zonal with increasing K_v in response to an anticyclonic shift of cold and warm features that extend through the entire water column but are most clearly seen in bottom buoyancy.

and not β that provides the main resistance to meridional flow. The effect of horizontal friction is small but weighs in on the side of *increased* meridional flow and buoyancy transport and a *decreased* pycnocline depth.

The relative importance of various processes in determining the overturning is also evident in the horizontal-averaged buoyancy plots of Fig. 2. Without rotation, viscosity alone permits an enormous rate of overturning leading to very warm deep water and a very shallow thermocline. With rotation, but without zonal boundaries, overturning is weak and the thermocline is deep, extending nearly to the bottom. Between these two extremes lie the β plane, f plane, and f plane in a reentrant y channel. The last experiment has doubled meridional extent (L_y = 10 000 km) and the boundary condition, (2.2), is extended to the periodic form:

$$Q_b = P\{2 \times 10^{-2}[1 + \cos(2\pi y/L_y)] - b[z = -25 \text{ m}]\}. \quad (3.5)$$

That this experiment, and the f-plane and β-plane box

TABLE 2. Maximum overturning and buoyancy transport sensitivity to β for $f_0 = 10^{-4}$ s^{-1}.

β (m^{-1} s^{-1})	Ψ (10^6 m^3 s^{-1})	F_b (10^4 m^4 s^{-3})
0	6.48	10.9
10^{-11}	5.84	9.55
2×10^{-11}	5.55	8.67

TABLE 3. Maximum overturning and buoyancy transport sensitivity to f_0 for $\beta = 2 \times 10^{-11}$ m^{-1} s^{-1}.

f_0 (s^{-1})	Ψ (10^6 m^3 s^{-1})	$\Delta \ln\Psi/\Delta \ln K_v$	F_b (10^4 m^4 s^{-3})	$\Delta \ln F_b/\Delta \ln K_v$
10^{-5}	21.3		27.7	
		−0.52		−0.41
10^{-4}	6.48		10.9	
		−0.37		−0.39
10^{-3}	2.76		4.49	

configurations, all have a very similar buoyancy structure indicates that the coarse-resolution model overturning and thermodynamic structure are primarily controlled by the adjustment of a uniformly rotating viscous fluid to boundaries parallel to the surface forcing gradient (the eastern and western boundaries).

Before moving on to examine this adjustment in some detail, it is worth noting that β does have an influence upon the distribution of upwelling. Figure 3 shows a meridional section of vertical velocity at midbasin for the f-plane and β-plane experiments. The β-plane upwelling is larger in the interior and smaller near boundaries than that of the f plane. Additionally, interior upwelling decreases moving poleward in the β-plane model. This is to be expected from the meridional decrease of Rossby wave speed ($\beta c^2/f^2$), as these waves are primarily responsible for bringing the upwelling into the interior.

4. Adjustment to boundaries

The adjustment of a baroclinic current normal to a coast on an f plane is initiated in a horizontal Ekman layer of thickness $(2A/f)^{1/2}$. Within this layer friction allows flow from high to low pressure parallel to the coast and upwelling or downwelling depending upon the direction of the baroclinic current. The essential role of friction in allowing vertical velocity is clear from the f-plane frictional geostrophic vorticity balance obtained by taking the curl of (2.1a) and substituting (2.1c):

$$f\frac{\partial w}{\partial z} + A\nabla^2\left(\frac{\partial v}{\partial x} - \frac{\partial u}{\partial y}\right) = 0. \qquad (4.1)$$

If the coastal region is stratified, the stratification will be lifted or depressed in the coastal Ekman layer. This tendency may be balanced by local diffusive processes, but in general density anomalies at the coast diffuse offshore by viscous diffusion and propagate in the Kelvin wave direction around the boundary (even though our model filters out all gravity waves, including Kelvin waves).

First, we will explore these processes with a linearized frictional geostrophic shallow water system:

$$-fv = -c^2\frac{\partial \eta}{\partial x} + A\frac{\partial^2 u}{\partial y^2} \qquad (4.2a)$$

$$fu = -c^2\frac{\partial \eta}{\partial y} + A\frac{\partial^2 v}{\partial y^2} \qquad (4.2b)$$

$$\frac{\partial \eta}{\partial t} + \frac{\partial u}{\partial x} + \frac{\partial v}{\partial y} = 0, \qquad (4.2c)$$

where the x direction is alongshore, the y direction is cross-shore, and c is the gravity wave speed (the height perturation η has been normalized by the reference depth). If we further assume no variations in the alongshore direction and alongshore geostrophy, we can easily derive an approximate equation for offshore diffusion of a coastal anomaly:

$$\frac{\partial \eta}{\partial t} + \frac{Ac^2}{f^2}\frac{\partial^4 \eta}{\partial y^4} = 0. \qquad (4.3)$$

This kind of diffusion involves Coriolis forces acting upon ageostrophic flow due to viscous entrainment. The dispersal of an anomaly with alongshore variation at the coast is considerably more complicated. Now we set up such a case in a 5000-km wide x channel. The linear model, (4.2), is integrated with $A = 10^6$ m^2 s^{-1}, $f = 10^{-4}$ s^{-1}, and $c = 2$ m s^{-1}. A high-resolution grid is used with x-direction resolution of 50 km and y-direction resolution of 25 km (with the above parameter values the Ekman layer thickness is 141 km). The

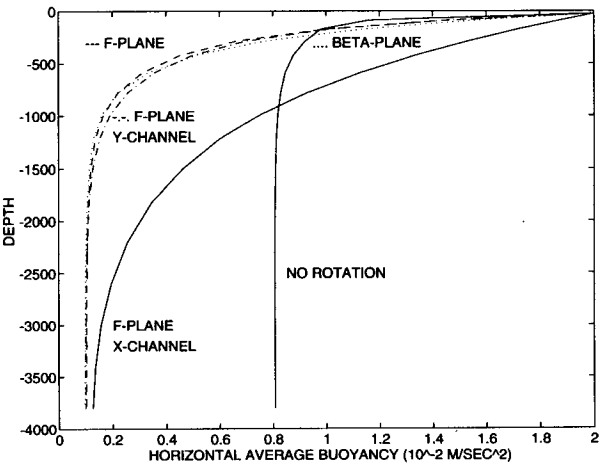

FIG. 2. Horizontal average buoyancy in steady-state circulations. The three nearly identical thermoclines for the β-plane, f-plane, and f-plane y-channel (reentrant in meridional direction) experiments fall between those of the no-rotation case and the f-plane x-channel (reentrant in zonal direction) case.

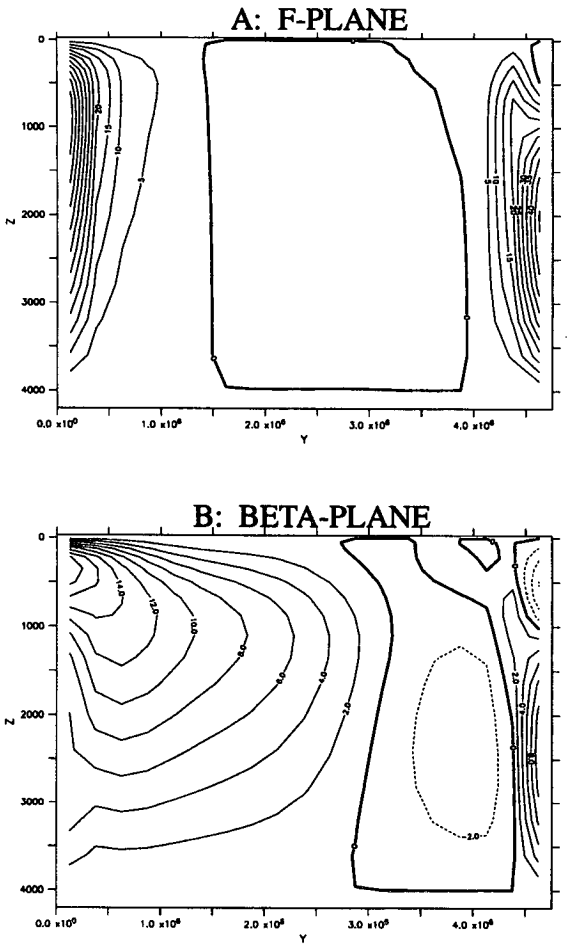

FIG. 3. Meridional section of vertical velocity (m yr^{-1}) at midbasin for f-plane (a) and β-plane (b) experiments. Rossby wave radiation brings greater upwelling into the interior in the β-plane case.

model is initialized with a Gaussian height depression with an offshore radius of 125 km and an alongshore radius of 250 km centered on the northern boundary. Thus, the depression is contained within the coastal Ekman layer.

Figure 4a shows the height anomaly at $t = 0$, $t = 1/4$, and $t = 1/2$ yr. In addition to the expected offshore diffusion, the depression propagates westward along the coast. There is considerable broadening of the initial shape in the alongshore direction such that the depression center propagates more slowly than the leading edge of the "wedge." Figure 4b shows height, u, and v velocities at the northernmost gridpoint where propagation is fastest. The alongshore velocity u has convergence centered upon a point just east of the depression center with greater speeds to the west where the wedge-shaped height field is contributing a larger geostrophic component to eastward flow. The cross-shore velocity is convergent upon a point just east of center and divergent well to the west (the direction of propagation). The cross-shore velocities are larger to the east, so the flow is oriented more parallel to the coast on the western side of the depression center.

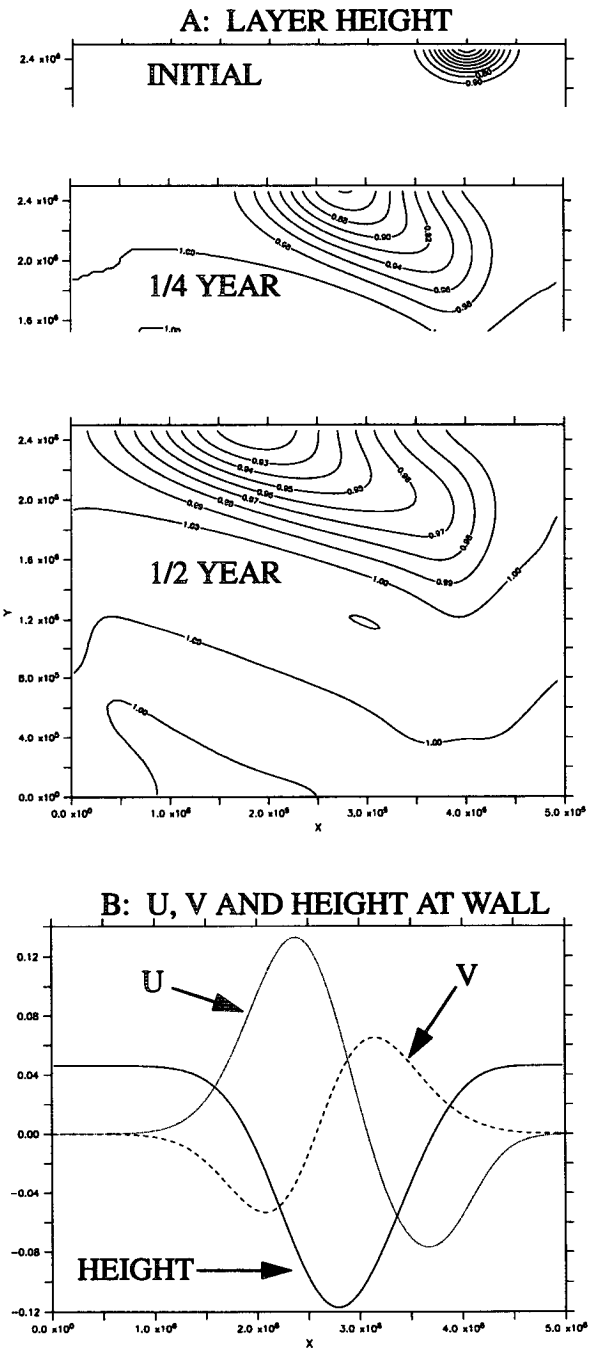

FIG. 4. Viscous boundary propagation in a shallow water linear frictional geostrophic model. A Gaussian depression contained in the coastal Ekman layer diffuses offshore and propagates in the Kelvin wave direction (a). The phase relations between the velocities and the layer height at the coast at $t = 1/4$ yr show that the cross-shore velocity (v) is responsible for the direction of propagation (b).

Although the propagation is rather complicated and clearly dispersive, we can scale it according to the following schematization. The depression at the coast diffuses into the interior setting up a geostrophic, cyclonic flow offshore. This flow diverges from the coast downstream of the original depression (with the coast on the right in the Northern Hemisphere) and converges onto the coast upstream, moving the depression in the Kelvin wave direction. If we neglect the alongshore flow, assume cross-shore geostrophy just outside of the Ekman layer of width $\Delta y = \sqrt{2A/|f|}$, and treat the convergence as occurring uniformly within the Ekman layer, we derive an approximate equation for nondispersive boundary propagation in the Kelvin wave direction,

$$\frac{\partial \eta}{\partial t} \approx -\frac{\partial v}{\partial y} \approx -\frac{c^2}{f}\frac{\partial \eta}{\partial x}\Big/\Delta y \approx -\frac{c^2}{f}\sqrt{|f|/2A}\,\frac{\partial \eta}{\partial x}. \tag{4.4}$$

With the chosen parameter values this gives a boundary propagation speed of 4.4×10^3 km/(1/2 yr). This is somewhat faster than the leading edge of the "wedge" and about twice the speed of the depression center in the numerical experiment. Equation (4.4) is closely related to an equation for numerical boundary waves on a C-grid discussed by Killworth (1985). Here the width of the coastal divergent layer is determined by Ekman layer dynamics rather than the offshore grid spacing. If the coastal Ekman layer is not resolved (as is the case in most coarse-resolution OGCMs) a numerical wave with a resolution-dependent propagation speed replaces the viscous boundary wave. The propagation characteristics of these numerical waves have been found to be similar to those of the viscous boundary waves discussed here. Winton (1993b) discusses a spindown experiment on a grid that does not resolve the horizontal Ekman layer in two models: one is similar to (2.1) and the other has a boundary parameterization that effectively filters out the numerical boundary waves (Winton and Sarachik 1993).

In steady OGCM solutions, the interior processes of convection and vertical diffusion combine with the meridional gradient of surface buoyancy fluxes to drive a zonal baroclinic circulation. This circulation is typically intensified in a jet located at high latitudes in the convective region (Fig. 1). The role of this jet in forcing the gyre circulations through the adjustment at zonal boundaries will now be examined by observing its spindown in an f-plane frictional geostrophic model. For this experiment we use the same values of A and f used in the boundary propagation experiment described above ($K_v = K_h = 0$). A horizontal resolution of 166 km (a 30 by 30 grid), although only marginally resolving the horizontal Ekman layer, was found to be sufficient to produce a convergence of boundary wave propagation speeds. The initial buoyancy structure,

$$b(y, z) = 2 \times 10^{-2}(1 - \exp[-(5 \times 10^6 - y)^2/(2 \times 10^6)^2])(1 - \exp[z/400]), \tag{4.5}$$

describes a Gaussian jet along the polar wall with a radius of 2000 km. The basic stratification away from the polar boundary gives a first baroclinic-mode gravity wave speed of 2 m s^{-1}. Figure 5 shows the evolution of thermocline level horizontal velocity and buoyancy at one-year intervals during the spindown. Wedge-shaped boundary waves can be seen passing cyclonically around the basin, encircling the cold water poleward with warm water and the warm water equatorward with cold water. After three years, the boundary jets have diffused significantly into the interior, and the setup of the cyclonic cold and anticyclonic warm gyres is well under way. The cold signal front has velocities oriented more parallel to the coast than the warm signal front as in the linear case described above. However, the faster propagation of the cold signal is not a linear effect. A linear model experiment with the same basin geometry, parameters, and initial jet structure was also performed. It showed similar propagation speeds for the two fronts (the linear model warm front advances in one year to its position at three years in the nonlinear model). The development of the cold gyre lags behind that of the warm gyre for one or both of the following reasons: 1) Since the initial stratification decays to zero at the northern boundary, the gravity wave speed is slower and there is slower boundary wave propagation in this region and 2) the east bearing upper jet opposes propagation of upper ocean buoyancy features.

How do these propagation characteristics leave their mark upon a steady circulation? To answer this question the above frictional geostrophic model is integrated to steady state with restored surface buoyancies as in section two. Larger values of K_v and K_h (10^{-4} m^2 s^{-1} and 10^3 m^2 s^{-1}) were used to eliminate any grid noise in preparation for the use of this model in variability studies in the next section. Figures 6a and 6d show the upper-ocean circulation is dominated by a warm anticyclonic gyre. The cold signal has spread cyclonically along the boundary from the poleward-west corner to a point nearly halfway up the eastern boundary to form this gyre. There is no counterpart cold gyre. The jet head has turned poleward somewhat along the eastern boundary in response to the accumulation of warm water at depth there. Away from the eastern boundary, the polar boundary is unstratified and steady convection to the bottom along with strong surface buoyancy loss combine to give the water column there a damping time of the ocean depth divided by the piston velocity, or about 11 years (4000 m/1 m day^{-1}). This prevents the propagation of boundary disturbances from developing the cyclonic flow seen in the jet spindown experiment. As a result, subduction along the eastern boundary forces a bowing down of the buoyancy contours deepening poleward (Fig. 7b) and a spectrum of warm intermediate and deep waters is pro-

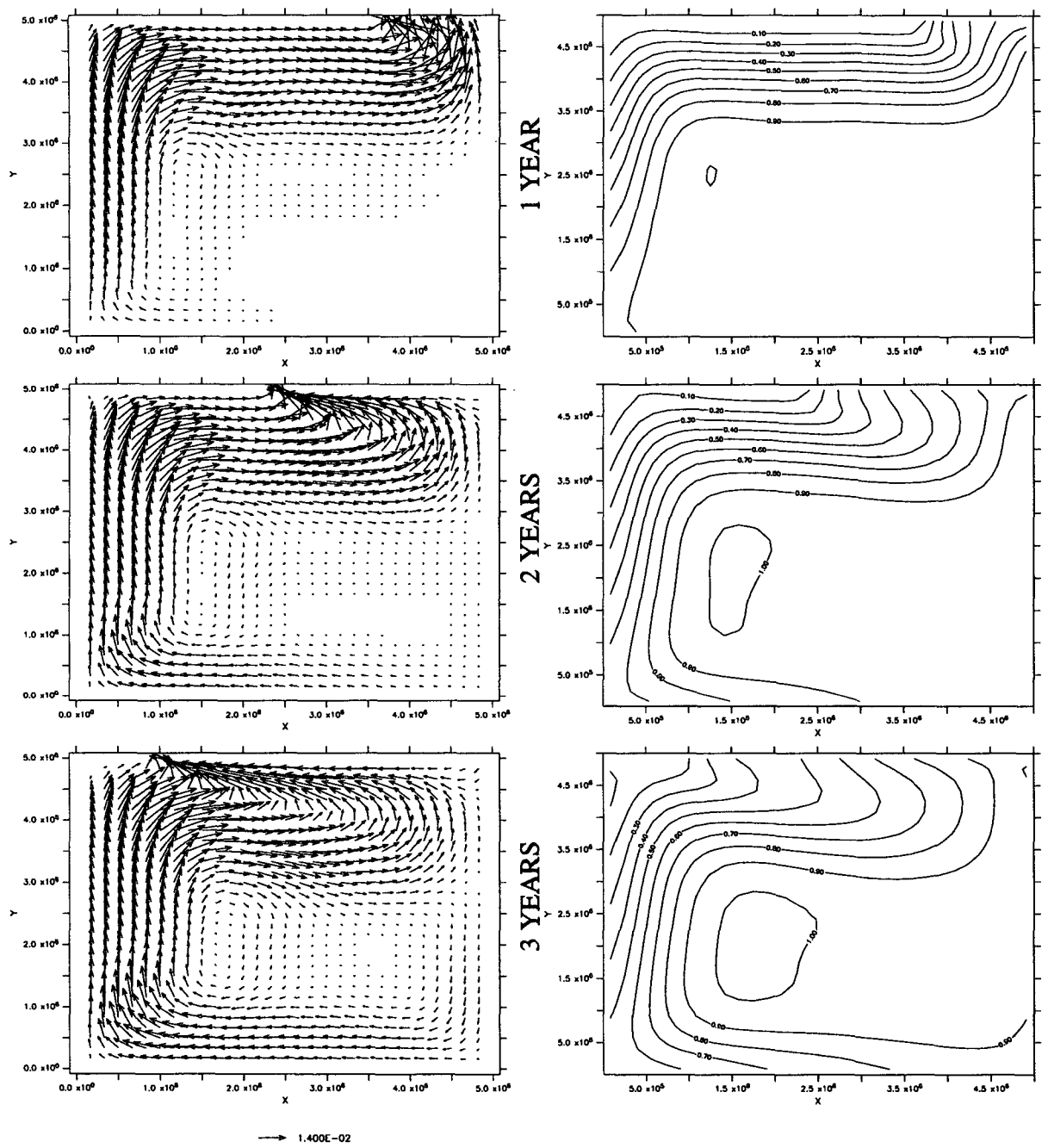

FIG. 5. Spindown of a zonal jet occupying the poleward 1/5 of an f-plane basin [Eq. (4.5)]. Horizontal velocities (left panels) and buoyancy (right panels) at $z = -287.5$ m. Viscous boundary waves set up a cyclonic (anticyclonic) gyre in the poleward (equatorward) part of the basin. Because of the stronger stratification, and hence faster propagation, the equatorward gyre sets up more rapidly. Velocity units are meters per second; buoyancy units are 10^{-2} meters per square second.

duced in the flow away from the boundary below (Fig. 6). The downwelling water on the eastern boundary is more buoyant than the water upwelling at comparable levels along the western boundary. Thus, the circulation that adjusts the zonal flow to the zonal boundaries converts kinetic energy to potential energy, the opposite of the meridional circulation, which has denser water in its sinking branch. The strongest sinking occurs in the poleward eastern corner in a column that does not convect to the bottom. The deep column of warm water that results produces a cyclonic circulation in the deep. The equatorward flank of this heads into the east-

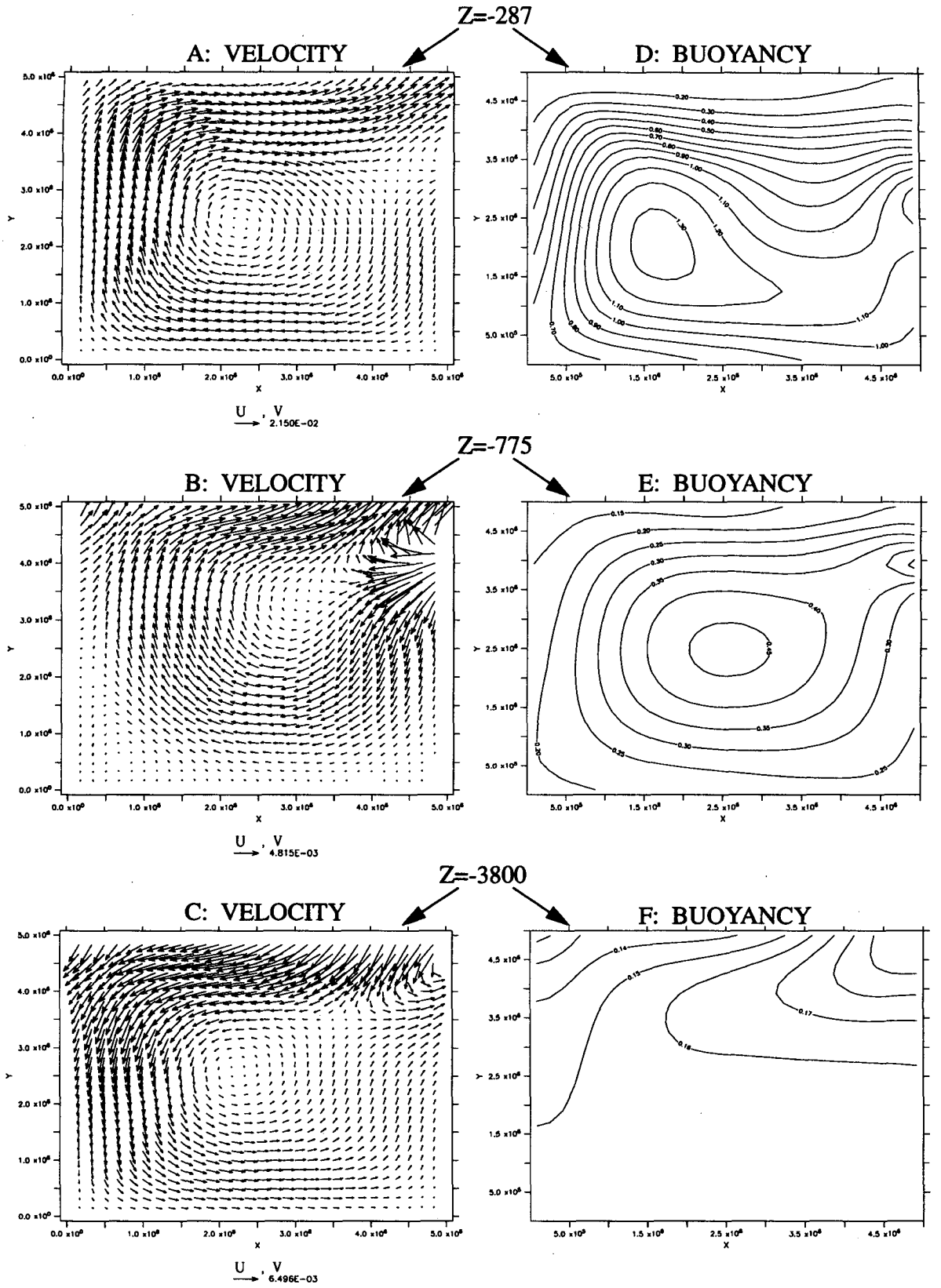

FIG. 6. Steady-state *f*-plane horizontal circulation (left panels) and buoyancy (right panels) at three levels. The lack of stratification along the northern boundary inhibits propagation and forces warm water to be subducted at the eastern boundary. Velocity units are meters per second; buoyancy units are 10^{-2} m s^{-2}.

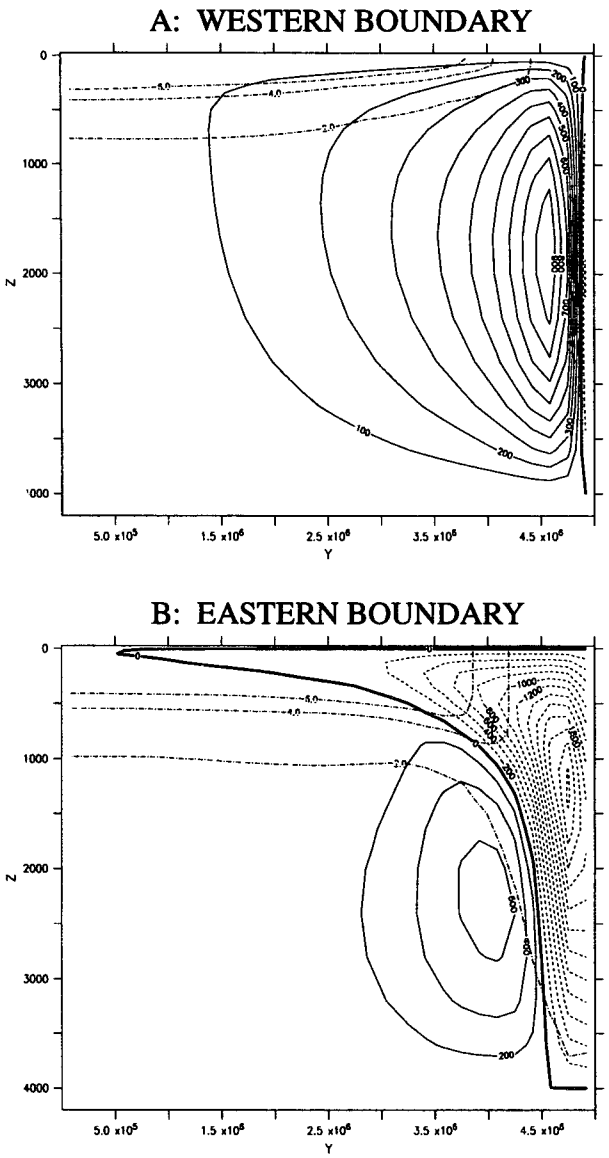

FIG. 7. Steady-state f-plane vertical velocity (m yr^{-1}) on east and west boundaries. Three buoyancy contours (2, 4, and 6 $\times$ 10^{-3} m s^{-2}) are superimposed as dot–dashed lines to show the warming due to sinking on the eastern boundary and corresponding cooling due to upwelling on the western boundary.

ern boundary forming the unexpected downwelling over upwelling circulation of Fig. 7b. The western boundary upwelling is strongest at midlevels beneath the jet tail and diminishes smoothly equatorward, consistent with the spread of the upwelling signal by fast propagating boundary disturbances. These features are characteristic of flat bottom OGCM solutions (e.g., Cox and Bryan 1984; Colin de Verdiere 1988). Eastern boundary subduction has also been shown to be the dominant source of Antarctic Intermediate Water in a coarse-resolution global model (England et al. 1993).

5. Fixed flux experiments

Now we replace the restoring boundary condition used to generate steady states with a fixed surface buoyancy flux boundary condition. This kind of boundary condition does not damp disturbances that might propagate along the polar wall. And we will see shortly that such disturbances are responsible for periodically releasing some of the warm water trapped on the poleward section of the eastern boundary. Consequently, the frictional geostrophic model solutions with steady fixed flux forcing are not steady but rather exhibit decadal-scale variability. The sequence of experiments below will show that boundary disturbances forced by thermal wind currents normal to weakly stratified coasts play a central role in this kind of variability. First, however, we can eliminate the possibility that the fixed flux variability is a meridional plane phenomenon related to the loop oscillators found with mixed boundary conditions (Welander 1986; Winton and Sarachik 1993). To do this we employ the two-dimensional frictional model of Winton (1995) with the fixed surface density boundary condition used in that study replaced with a fixed density flux boundary condition. We have already derived a scaling for the overturning associated with a fixed surface density gradient in this model [Eq. (3.4)]. This scaling is the same as the equivalent scaling for the rotating model (3.1c) with r replacing f, so the sequence of steps that led to the fixed flux scaling, (3.3), for the rotating model leads to a similarly analogous scaling for the frictional model:

$$\Psi \approx \left[\frac{K_v^2 F_b L}{r}\right]^{1/4}, \quad \Delta b \approx \left[\frac{F_b^3 r}{K_v^2 L}\right]^{1/4}. \quad (5.1a,b)$$

Now we perform experiments to determine if these scales hold and if spontaneous variability arises under strong fixed flux forcing. Table 4 shows the result of forcing the model with half-cosine-shaped density fluxes in a range of magnitudes (equivalent to buoyancy fluxes multiplied by a factor ρ_0/g). The weakest forcing produced a steady overturning with a nondimensional magnitude near the 1.6 $\times$ 10^{-2} value of the Winton (1995) standard case. This standard case gave a pycnocline scale similar to that observed in the ocean. The strongest forcing produced a steady overturning more than twice the Winton (1995) standard case. In

TABLE 4. Maximum overturning and density range sensitivity to F_d (2D model).

F_d	Ψ	$\Delta \ln\Psi/\Delta \ln F_d$	$\Delta\rho$	$\Delta \ln\Delta\rho/\Delta \ln F_d$
10^{-2}	1.3 $\times$ 10^{-2}		0.47	
		0.34		0.72
4 $\times$ 10^{-2}	2.1 $\times$ 10^{-2}		1.26	
		0.32		0.71
0.16	3.3 $\times$ 10^{-2}		3.38	

all three experiments the circulations rapidly approached steady state with only a very weak overshooting behavior. The model determined overturning sensitivity is closer to $\Psi \sim F_b^{1/3}$ than the $\Psi \sim F_b^{1/4}$ from the scaling argument. The buoyancy range (density range multiplied by g/ρ_0) has only slightly less than the predicted sensitivity of $\Delta b \sim F_b^{3/4}$. The main point, however, is that with this meridional plane model the fixed flux forcing produced steady circulations in rough agreement with the scaling argument even when relatively strong forcing was applied.

Returning now to the three-dimensional frictional geostrophic model, we use the boundary condition

$$Q_b = F\cos(y\pi/L_y) \tag{5.2}$$

with F set to 10^{-8} m^2 s^{-3}, based roughly upon the buoyancy transport of the model with restored surface buoyancies (the f-plane steady state presented in the last section). As in that experiment, a 30 by 30 grid is used and the model is configured with $A = 2.5 \times 10^5$ m^2 s^{-1}, $K_h = 5 \times 10^2$ m^2 s^{-1}, $K_v = 5 \times 10^{-5}$ m^2 s^{-1}, and $f = 10^{-4}$ s^{-1}. A β-plane version has $f_0 = 10^{-4}$ s^{-1} and $\beta = 2 \times 10^{-11}$ m^{-1} s^{-1}. With the above boundary condition, both β-plane and f-plane configurations of the model exhibit self-sustaining oscillations with a period of about 50 years (Fig. 8). The variability is large amplitude—the maximum meridional overturning at midbasin in the β-plane case, for example, varies between less than 5 Sv (Sv $\equiv 10^6$ m^3 s^{-1}) and more than 8 Sv. Inspection of the details of the variability revealed that they were basically the same in the two models, so for simplicity the f-plane oscillation is presented here.

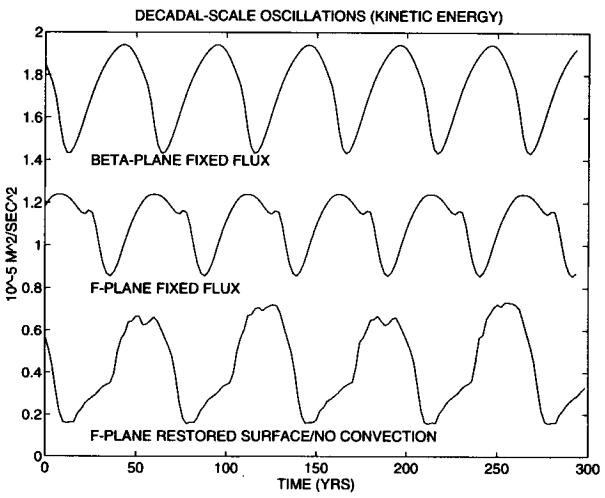

FIG. 8. Kinetic energy variability for β-plane and f-plane experiments forced with fixed surface buoyancy fluxes (upper curves) and f-plane experiment with restored surface buoyancies but no convective adjustment. Reduced damping in these experiments allows viscous boundary disturbances to propagate cyclonically around the basin perimeter. The mean kinetic energy is arbitrary.

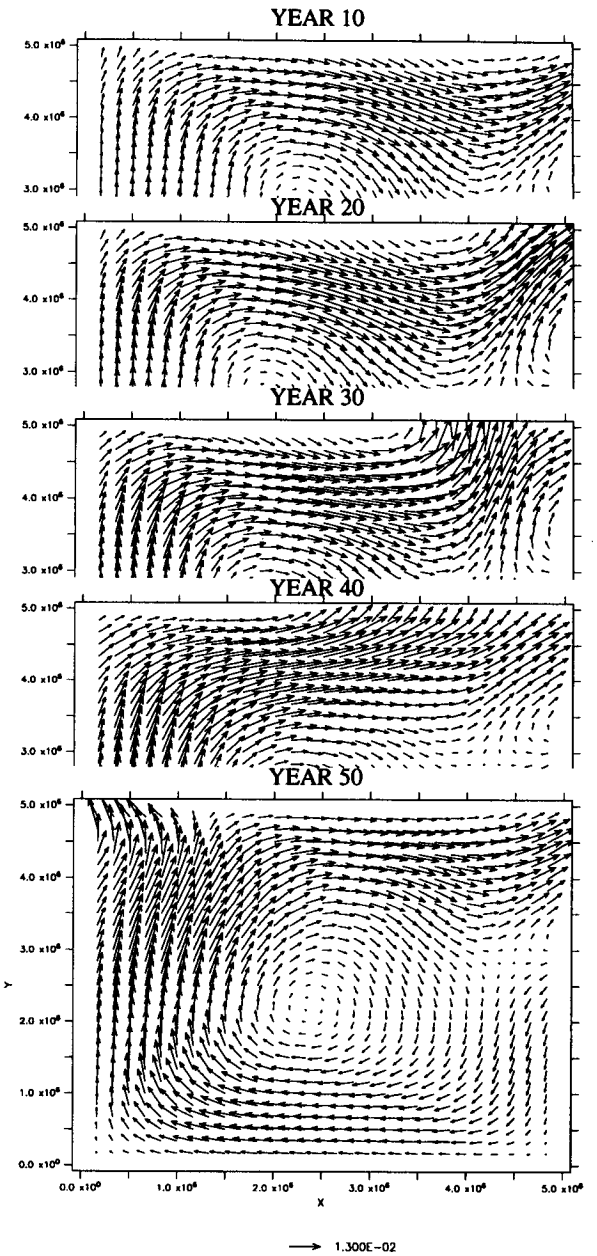

FIG. 9. The f-plane oscillation horizontal velocity at $z = -287.5$ m. A cyclonic cold anomaly builds up in the poleward-east corner just poleward of an anticyclonic warm anomaly. This couple propagates slowly westward along the polar boundary. This leg of the propagation consumes most of the 50-yr period of the oscillation. Velocity units are m s^{-1}.

Figure 9 shows thermocline level velocities at 10-year intervals over a 40-year segment of the f-plane oscillation cycle. In the 10 years prior to the top panel, upward surface buoyancy flux has formed a lobe of cold water along the eastern part of the polar boundary—the region most remote from western boundary current warm advection. A warm boundary disturbance

having rounded the basin arrives on the poleward section of the eastern boundary between the top two panels of Fig. 9. An intensified jet heads into the coast, between the cold cyclonic circulation poleward and the warm anticyclonic circulation equatorward. As the buoyancy gradient across this jet increases, it begins to propagate slowly in the cyclonic direction along the coast. As it passes westward along the polar boundary, cold unstratified water is swept away and replaced with the warm stratified water in its wake. The warm water on the boundary after passage reduces the offshore baroclinity resulting in a weakening of the alongshore current. This effect is the source of the variability in kinetic energy shown in Fig. 8. The minimum kinetic energy is attained when the anamolously warm water has spread along the western boundary (about 10 years after the bottom panel of Fig. 9). The warm signal continues to propagate cyclonically around the basin eventually reaccumulating in the eastern boundary warm water pool just south of the northern boundary (the bowed downward buoyancy contours of Fig. 7b). The propagating disturbance resembles the linear boundary wave discussed in the last section, but there is the important difference that the water ahead of the oscillating model disturbance is largely unstratified, and since there are large horizontal buoyancy gradients, horizontal advection is likely also playing a role. The propagation is also similar to that of the disturbance passing along the northern boundary in the jet spindown experiment of the last section although the propagation speed is slower in the reduced stratification under continuous forcing in the present case. After warm water has moved west in the wake of the disturbance, the eastern boundary warm pool weakens and moves slowly southward. The impression from animations is of this pool weaving in the meridional direction, casting off a warm boundary disturbance along the polar boundary at the polewardmost point in its traversal.

That the oscillation is captured by f-plane dynamics allows us to narrow down its root cause by modifying the basin configuration and forcing structure, and then noting the presence or absence of the variability. The configurations explored and results obtained are summarized in Fig. 10 (configuration e is the standard experiment). By removing the east and west boundaries from the standard experiment (configuration a in Fig. 10) we can determine if some sort of baroclinic instability, potentially aided by frictional interaction with the polar boundary, is the cause of the oscillations. The steady circulation that results shows that this is not likely to be the case.

A particularly interesting forcing configuration is the square symmetric pattern (b and d in Fig. 10),

$$Q_b = F\{\sin(x\pi/L_x)\sin(y\pi/L_y) - 0.4057\}, \quad (5.3)$$

where the constant is used to set the net buoyancy flux to zero. With cooling at the edges ($F = -10^{-8}$ m^2 s^{-3}), the oscillations produced by this forcing consist of a single jetlike perturbation, normal to the coast, passing cyclonically around the basin in a manner similar to that of the disturbance shown in Fig. 9. Cold water, which accumulates in the corners, is flushed out by the passage of this disturbance. The disturbance takes about one hundred years to traverse the entire perimeter but the kinetic energy goes through a complete cycle with the traversal of each edge. The minimum in kinetic energy occurs when the warm signal reaches the center of an edge and the maximum occurs when the disturbance jet is aimed into a corner. A quasi-steady state with cold water forming a triangle in each of the four corners existed prior to the growth of the propagating disturbance. The same forcing pattern with warming on the edges ($F = 10^{-8}$ m^2 s^{-3}) produced a steady state.

From these experiments it might be concluded that corners are critical to the oscillations. To test whether or not this is the case a double length ($L_y = 10^7$ m) channel, reentrant in the y direction, was forced with the periodic surface forcing,

$$Q_b = F\cos(2\pi y/L_y), \quad (5.4)$$

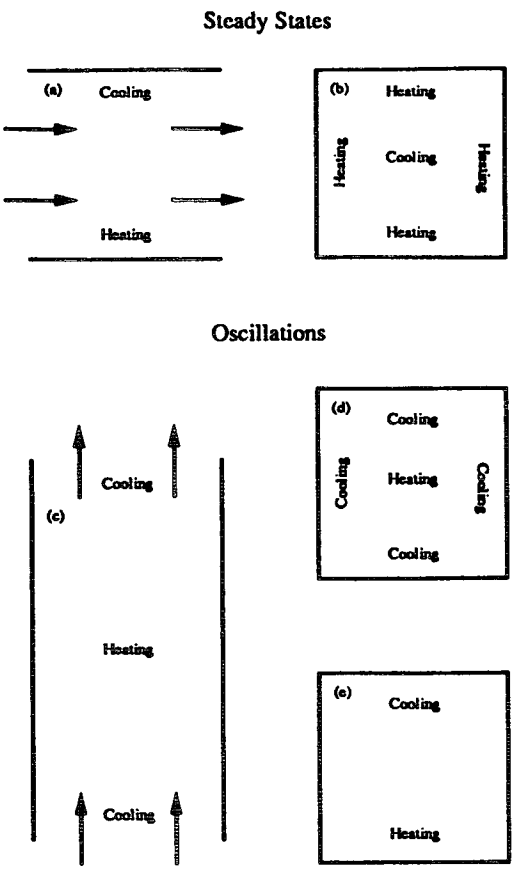

FIG. 10. Oscillating and nonoscillating f-plane configurations under fixed buoyancy flux forcing. Critical to the presence of oscillations is the forcing of thermal wind currents normal to weakly stratified coasts.

with $F = -10^{-8}$ m^2 s^{-3} (c in Fig. 10). Eighty-year period oscillations resulted. The oscillation is antisymmetric about midbasin ($x = L_x/2$). On the eastern and western boundaries, warm bowl-like structures similar to the one depicted by the dash–dotted lines in Fig. 7b, are maintained by onshore upper flow of zonal jets. These move up and down the coast as they amplify and decay in a manner similar to that of the corresponding structure in the standard experiment.

Why do oscillations occur with the fixed flux boundary condition and not with the restoring boundary condition (2.2)? A fixed flux boundary condition requires that the circulation develop interior buoyancy divergences to match the surface boundary condition. It is possible that some aspect of the dynamics prohibits this from being effected by a steady circulation. The substantial horizontal diffusivity and the smooth form for the surface fluxes used in the above experiments make this seem less likely. Furthermore, experiments have been performed that indicate that the aspect of the model formulation critical to oscillations is weak damping rather than the constraint on interior buoyancy divergence. The bottom curve of Fig. 8 shows oscillations produced by turning off the convective adjustment in the f plane experiment of section 4, shown in Figs. 6 and 7. Without convection the water column damping timescale for thermal anomalies is no longer controlled by the surface boundary condition (which gives an order 10-yr timescale) but reverts to a much longer diffusive timescale. Transient oscillations have also been found with convective adjustment and a restoring boundary condition but with the restoring piston velocity reduced by a factor of 10 and the reference buoyancy range increased by a factor of 4. It appears that the weak high-latitude damping in these experiments permits boundary disturbances to propagate across the polar boundary, thereby allowing decadal-scale variability to occur.

6. Discussion

This paper has emphasized the viscous adjustment of baroclinic currents to coasts and the role of propagating boundary disturbances in that adjustment. The importance of this adjustment is evident in the sensitivities of the model—in particular, the large sensitivities to f and the presence or absence of zonal boundaries and the small sensitivities to β, A, and the presence or absence of meridional boundaries. Although the customary choice of horizontal viscosity does not permit coarse-resolution grids to resolve the viscous boundary layer where viscous boundary wave propagation occurs, the physical wave is replaced by a numerical wave that has been found through experimentation with the model to have similar propagation characteristics. These boundary waves play an important role in both steady and oscillating solutions of the coarse-resolution models.

Although the sensitivity of overturning magnitude (as determined from the midbasin maximum) to vertical diffusivity is apparently under thermodynamic control leading to general agreement between the rotating model used here and nonrotating two-dimensional model of Winton (1995), the details of high-latitude circulation in the rotating model are better understood in terms of propagating warm and cold anomalies arrested by the mean flow. These anomalies play a role in the change in orientation of the high-latitude jet with vertical diffusivity that contaminated the basin maximum streamfunction, making it an unsuitable measure of thermodynamically important upwelling. The baroclinic circulation between these deep anomalies is similar to the circulation between the propagating cold/warm feature of the decadal-scale oscillations discussed in section 5 but on a broader, basinwide, scale (cf. Figs. 1 and 9). The most straightforward explanation of the anticyclonic shift of these features with increased diffusivity is that it is due to the stronger anticyclonic upper circulation in the higher diffusivity case (advection by the upper flow may be more effective because of the small buoyancy gradients in the deep). Boundary propagation in the weakly stratified high-latitude water column is very nonlinear, so it is difficult to advance beyond this speculation.

Under fixed buoyancy flux boundary conditions decadal-scale oscillations are found with a number of forcing and basin configurations that have in common forcing of thermal wind currents normal to weakly stratified coasts. The propagation of a boundary disturbance is easily tracked around the basin perimeter with particular activity in the warm water along the poleward section of the eastern boundary. The oscillations do not have direct geophysical relevance because of the unrealistic surface boundary condition but may serve as a bridge to understanding the complicated decadal-scale variability that occurs in models forced with mixed boundary conditions[1] (restored surface temperatures and fixed surface salt fluxes) and coupled ocean–atmosphere simulations. Elements of the boundary propagation of disturbances originating from the warm water along the poleward eastern boundary may be found in the decadal-scale mixed boundary condition variability described by Weaver and Sarachik (1991) and Yin and

[1] The decadal-scale variability is one of the three kinds of internal variability found in mixed boundary condition models. The other two are advective "loop" oscillations and "deep decoupling oscillations," which involve alternating periods of basinwide diffusive warming and advective cooling (see Winton and Sarachik 1993, and references therein). Of the three kinds only the decadal-scale variability has not been reproduced in two-dimensional models.

Sarachik (1995). Figure 10 of Weaver and Sarachik shows a subthermocline anticyclone near the poleward eastern boundary similar to that depicted in Fig. 6b. The flow along the polar boundary on the poleward flank of this feature switches from eastward to westward in a signal that appears to propagate west along the polar boundary. Their Fig. 11 shows that a strong warm/cold couple on the eastern boundary dissipates as this sequence of circulation changes progresses. A similar weakening of the eastern boundary baroclinity occurs as the disturbance depicted in Fig. 9 of this study passes west along the polar boundary. Figure 9 of Yin and Sarachik depicts a sequence of thermocline level velocities with an onshore jet propagating from just equatorward of the polar boundary on the eastern boundary cyclonically to some distance westward along the polar boundary.

Why might we expect the fixed flux experiments to be relevant to the mixed boundary condition experiments? Yin and Sarachik show that an important element of the forcing of mixed boundary condition decadal variability is strong freshening along the polar boundary (this was also a feature of the Weaver and Sarachik forcing). Such forcing will tend to suppress convection along this boundary. As shown in the last section, without convection the water column damping timescale is increased sufficiently to allow oscillations to occur (Fig. 8, bottom curve). Thus, weak damping is a characteristic that a polar boundary without convection and a polar boundary under fixed buoyancy flux forcing hold in common that permits boundary disturbances to propagate across the basin. When this happens, there is the potential for the warm water mass formed by eastern boundary subduction to influence the energetic western boundary current. As this current is the primary transporter of heat and salt in the models, variability due to the propagating boundary disturbances may induce variability in these quantities as well and, as a further consequence, convective variability. Studies of mixed boundary condition decadal variability typically focus upon the interplay of heat and salt in producing advective and convective variability, but the fixed flux experiments suggest that these interactions may not be causal.

In addition to weak damping, experiments with various basin and forcing configurations point to forcing of thermal wind currents perpendicular to coasts with weak stratification as an important factor in decadal-scale variability. The cross-shore baroclinity produced by this forcing is the generation mechanism for slowly propagating boundary disturbances. There are reasons to believe that such large-scale baroclinity is overestimated by the coarse-resolution models. From the mechanistic point of view, we expect that baroclinic eddies will draw some portion of the available potential energy out of the large-scale baroclinity. The absence of these instabilities along with inadequate representation of surface forcing and interactions with bottom topography may be contributing factors to the unrealistic confinement of water mass formation to coastal regions in the coarse-resolution models. Perhaps the most dramatic example of this comes from the England et al. (1993) study of Antarctic Intermediate Water formation. In their global model, the low salinity signature of this water mass radiates out from the southern tip of South America where low salinities are brought down from the surface by subduction and then advected into the interior by an intermediate level circulation (the Pacific branch of this is similar to Fig. 6b). This is in contrast to the actual distribution of salinity in the ocean, which has a low salinity tongue stretching from the surface in the circumpolar belt northward beneath the thermocline at all longitudes.

Figure 7b shows that the model deep water is formed by the same boundary subduction process. The deep warm feature that results has no counterpart in the observations of deep-water formation discussed by Killworth (1983). It seems likely that such a feature would be very susceptible to mixing by instabilities. Since this feature plays an important role in the decadal-scale oscillations presented here, the applicability of this kind of variability to the actual ocean must remain in doubt until the effects of instabilities can be accounted for.

Acknowledgments. Comments on the manuscript by Dr. Fenglin Yin, David McDermott, and two anonymous reviewers are gratefully acknowledged. This research was supported by a UCAR ocean modeling postdoctoral fellowship and grants from the NOAA/Office of Global Programs Atlantic Climate Change Program to the University of Washington Experimental Climate Forecast Center. FERRET, a diagnostics and graphics tool, was used extensively in the production of this paper.

REFERENCES

Bryan, F., 1987: Parameter sensitivity of primitive equation ocean general circulation models. *J. Phys. Oceanogr.*, **17**, 970–985.

Bryan, K., 1991: Poleward heat transport in the ocean. *Tellus*, **43AB**, 104–115.

Chen, F., and M. Ghil, 1995: Interdecadal variability of the thermohaline circulation and high-latitude surface fluxes. *J. Phys. Oceanogr.*, **25**, 2547–2568

Colin de Verdiere, A., 1988: Buoyancy driven planetary flows. *J. Mar. Res.*, **46**, 216–265.

——, 1989: On the interaction of wind and buoyancy driven gyres. *J. Mar. Res.*, **47**, 599–633.

Cox, M. D., and K. Bryan, 1984: A numerical model of the ventilated thermocline. *J. Phys. Oceanogr.*, **14**, 674–687.

Dellworth, T., S. Manabe, and R. J. Stouffer, 1993: Interdecadal variability of the thermohaline circulation in a coupled ocean–atmosphere model. *J. Climate*, **6**, 1993–2011.

England, M. H., J. S. Godfrey, A. C. Hirst, and M. Tomczak, 1993: The mechanism for Antarctic Intermediate Water re-

newal in a World Ocean model. *J. Phys. Oceanogr.*, **23,** 1553–1560.

Greatbatch, R. J., and S. Zhang, 1995: An interdecadal oscillation in an idealized ocean basin forced by constant heat flux. *J. Climate,* **8,** 81–91.

Haney, R. L., 1971: Surface thermal boundary conditions for ocean circulation models. *J. Phys. Oceanogr.*, **1,** 241–248.

Huang, R. X., and R. L. Chou, 1994: Parameter sensitivity study of the saline circulation. *Climate Dyn.*, **9,** 391–409.

Killworth, P. D., 1983: Deep convection in the world ocean. *Rev. Geophys.*, **21,** 1–26.

——, 1985: A two-level wind and buoyancy driven thermocline model. *J. Phys. Oceanogr.*, **15,** 1414–1432.

Weaver, A. J., and E. S. Sarachik, 1991: Evidence for decadal variability in an ocean general circulation model: An advective mechanism. *Atmos.–Ocean,* **29,** 197–231.

Welander, P., 1971: The thermocline problem. *Philos. Trans. Roy. Soc. London,* **A270,** 415–421.

Winton, M., 1993a: Deep decoupling oscillations of the oceanic thermohaline circulation. *Ice in the Climate System,* NATO ASI Ser., W. R. Peltier, Ed., Springer-Verlag, 417–432.

——, 1993b: Numerical investigations of steady and oscillating thermohaline circulations. Ph.D. dissertation, University of Washington, 155 pp.

——, 1995: Why is the deep sinking narrow? *J. Phys. Oceanogr.*, **25,** 997–1005.

——, and E. S. Sarachik, 1993: Thermohaline oscillations induced by strong steady salinity forcing of ocean general circulation models. *J. Phys. Oceanogr.*, **23,** 1389–1410.

Yin, F. L., and E. S. Sarachik, 1995: On interdecadal thermohaline oscillations in a sector ocean general circulation model: Advective and convective processes. *J. Phys. Oceanogr.*, **25,** 2465–2484.